PAPER

Check for updates

Structure–property correlations in piracetam polytypes†

Pratik P. Upadhyay, [iD] [a] Manish Kumar Mishra, [b]
Upadrasta Ramamurty [cd] and Andrew D. Bond [iD] ‡*[a]

Polymorphs II and III of piracetam exhibit a polytypic relationship comprising identical layers of molecules with different relative arrangements. Polymorph II has an interlayer structure in which the piracetam molecules adopt face-to-face and edge-to-edge alignments, while polymorph III adopts a herringbone type arrangement in the interlayer region. The structures are analysed using energy-vector models derived from *PIXEL* pairwise intermolecular interaction energies. Thermal expansion measurements show that the principal expansion axes are approximately aligned with the unit-cell axes in polymorph III, corresponding to directions within the polytypic layers and perpendicular to them. Expansion perpendicular to the layers is almost twice as large as that along any direction within the layers. Polymorph II shows greater volumetric expansion than polymorph III, and its principal expansion axes are aligned parallel and perpendicular to the planes of the piracetam molecules, rather than along the unit-cell axes. Nanoindentation experiments performed on single crystals along the direction perpendicular to the polytypic layers show that the polymorphs have similar hardness (H) values, but polymorph III has a significantly larger elastic modulus (E). Along the direction nearly parallel to the polytypic layers, polymorph II shows a very similar E value to that perpendicular to the layers, but a significantly smaller H value, implying easier slip between the polytypic layers. The tableting behaviour of bulk polymorph II is superior to that of polymorph III, suggesting greater plasticity for polymorph II, which is likely due to a greater degree of slip.

Introduction

Developing a robust understanding of the relationships between crystal structure and macroscopic physical properties can provide a rational basis for the design of crystalline chemical products for enhanced processability and performance, for example in the pharmaceutical industry.[1] To achieve this in any general sense requires understanding and control over a range of scales, from the single-crystal to particle and bulk levels. Concepts of crystal engineering can often be applied at the single-crystal level to modify, and

sometimes specifically to enhance, relevant materials properties.[2–5] To build knowledge in this area, it can be especially useful to study polymorphs, since these provide an opportunity to experiment with the same chemical system in different crystalline arrangements. Often, polymorphs exhibit structural differences in three dimensions, but in some cases, they retain a greater degree of structural similarity. For example, we have studied several pharmaceutically-relevant polytypic systems, in which consistent two-dimensional layers of molecules are arranged in different ways, including aspirin,[6] felodipine[7] and piroxicam.[8] We have observed twinning and "intergrowth polymorphism" in these systems, which can lead to variations in the physical properties of crystals on account of differing microstructures.

Over the last decade or so, nanoindentation has emerged as a powerful technique to examine the mechanical properties of molecular single crystals.[9–11] With it, one can determine elastic modulus (E) and hardness (H) of crystals obtained from typical small-scale crystallization trials. The results obtained have been correlated to bulk properties for a range of molecular crystals, including active pharmaceutical ingredients (APIs).[12–15] In the context of tableting of APIs, average H and E values are typically compared with elastic recovery or tabletability of a bulk powder.[16,17] One advantage

[a] *Department of Pharmacy, University of Copenhagen, Denmark*
[b] *Department of Pharmaceutics, College of Pharmacy, University of Minnesota, Minneapolis, Minnesota 55455, USA*
[c] *School of Mechanical and Aerospace Engineering, Nanyang Technological University, Singapore 639798, Republic of Singapore*
[d] *Institute of Materials Research and Engineering, Agency for Science, Technology and Research (A*STAR), 138634 Singapore*
† Electronic supplementary information (ESI) available: Details of *PIXEL* calculations, crystal face indexing, calculation of thermal expansion coefficients, AFM images of indentation impressions. See DOI: 10.1039/d0ce01694b
‡ Current address: University of Cambridge, Department of Chemistry, Lensfield Road, Cambridge, CB2 1EW, UK. Email: adb29@cam.ac.uk.
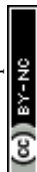
of nanoindentation is that it can probe crystals from several directions (dependent on the crystal faces that can be developed during crystallization), allowing an examination of the interaction anisotropy.[6] Measuring H and E values by nanoindentation for structurally related polymorphs provides experimental data that can be used to relate mechanical properties to crystal structure, and hopefully to link this understanding to bulk tableting behaviour.

In this paper, we examine the connections between structure and the physical and mechanical properties of a model API: piracetam (Fig. 1). Several polymorphs of piracetam have been reported,[18–28] of which forms II and III (denoted FII and FIII hereafter) are known to be stable at room temperature. Other polymorphs (forms I, IV, and V) are stable only at higher temperatures and/or pressures. The crystal structures of FII and FIII (CSD refcodes: BISMEV11 and BISMEV12) have previously been examined in detail.[29] They display a polytypic relationship, and our aim here is to examine the physical and mechanical properties of these polytypes. The relationship between the indentation responses and the closely-related crystal structures are considered using energy-vector models derived from *PIXEL* pairwise intermolecular interaction energies.[30] Thermal expansion measurements are also made to provide an additional experimental probe of the interaction anisotropy, which can add to the static picture of the energy-vector model. The results are finally compared to measurements of powder tabletability for the bulk samples.

Experimental

Materials

Piracetam was purchased from Fagron, Denmark and was received as FIII, as confirmed by powder X-ray diffraction (PXRD). HPLC grade solvents were used for crystallisation of single crystals and bulk powder samples.

Crystallisation of the piracetam polytypes

Single crystals of FII (block morphology) and FIII (plate morphology) were concomitantly grown by slow cooling of a hot saturated solution of piracetam in *n*-propanol at room temperature. The bulk powder of FII was prepared by heating the as-supplied FIII in an oven at 120 °C for 24 hours followed by slow cooling to room temperature. The powder was allowed to stand at room temperature for 48 hours, and the polymorphic purity of FII was confirmed by PXRD (ESI†).
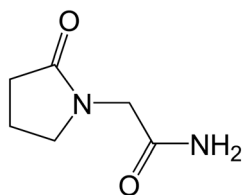

Fig. 1 Piracetam.

Single-crystal X-ray diffraction

The identity of single crystals of FII and FIII was confirmed by comparing the experimentally measured unit-cell parameters to those reported in the Cambridge Structural Database (CSD).[31] X-ray diffraction was carried out on a Bruker D8-QUEST instrument equipped with an Incoatec IµS Cu microsource. Face indexing was performed within the *APEX3* software (ESI†).

Powder X-ray diffraction (PXRD)

Powder X-ray diffraction (PXRD) data were collected on a Panalytical X'Pert Pro instrument equipped with a *PIXcel* detector using non-monochromated CuKα radiation (λ_{ave} = 1.5418 Å). Samples were placed on a zero-background Si holder and measured in reflection geometry, with sample spinning, over a 2θ range of 5 to 35°.

Thermal expansion measurements

Lattice parameters were measured for single crystals of FII and FIII over the temperature range *ca.* 100–300 K at 50 K intervals on a Bruker D8-QUEST single-crystal instrument (ESI†). Thermal expansion coefficients and directions of the principal expansion axes were calculated using the *PASCal* web tool.[32] Thermal expansion coefficients are quoted in ppm with units K^{-1}.

Nanoindentation

Good quality dried single crystals of FII and FIII, identified using a polarising microscope, were fixed on metal discs using a thin layer of epoxy resin (ESI†). Nanoindentation was performed in the direction normal to the crystal surface using a nanoindenter (Hysitron Triboindenter, Minneapolis, USA), equipped with an *in situ* AFM imaging capability. A three-sided pyramidal Berkovich diamond indenter (Poisson's ratio = 0.07, tip radius ≈ 100 nm) was used. A maximum force of 5 mN was applied with a loading indentation speed of 0.5 mN s^{-1}. At the maximum peak load of 5 mN, the tip was held for 30 s to ensure complete plastic deformation of the material, then unloading was applied at a rate of 0.5 mN s^{-1}. At least 15 indentations were performed on each crystal face to obtain consistent and reliable average data. The elastic modulus (E) and indentation hardness (H) were calculated from the unloading curve using the Oliver–Pharr method.[33,34] Where significant pile-up was observed during indentation, the H value was determined from the maximum load (5 mN) divided by the contact area, A, estimated from the AFM images of the indentation impressions (ESI†).[35,36]

Tablet preparation

Tablets of approx. 100 mg were prepared by compressing pure piracetam powders using a Gamlen single-punch laboratory tablet press. Flat-faced punches of 6 mm diameter were used with a compression speed of 60 mm min^{-1} using a 500 kg load cell. Prior to compression, the punch and die

Table 1 Crystallographic details of the piracetam polytypes[29]

Polymorph	Symmetry	Unit-cell parameters [Å, °]
FII	Triclinic	$a = 6.353$, $b = 6.528$, $c = 8.372$
(BISMEV11, transformed)	$P\bar{1}$	$\alpha = 80.30$, $\beta = 101.77$, $\gamma = 90.95$
FIII	Monoclinic	$a = 6.454$, $b = 6.386$, $c = 16.181$
(BISMEV12)	$P2_1/n$	$\beta = 92.06$

cavity were pre-lubricated using 1% magnesium stearate in acetone. The crushing strength of the tablets was measured on the same instrument using a 50 kg load cell. The strength (σ_c) of the tablets was calculated from the force required for crushing, F (N):

$$\sigma_c = (2F)/(\pi \cdot d \cdot t)$$

where d is the diameter of the tablet (mm), and t is the thickness of the tablet (mm). The units of σ_c are N mm^{-2} (= MPa). Post-tableting, the tablet was examined using PXRD to confirm that there was no occurrence of stress-induced phase transformation during tableting.

Computational methods

As a preliminary step, the crystal structures[29] of FII and FIII were energy-minimised using dispersion-corrected density functional theory (DFT-D) calculations. Prior to minimisation, the positions of all H atoms were normalised using the default settings in *Mercury*.[37] The calculations were made using *CASTEP*[38] *via* the interface in *Materials Studio*.[39] The PBE exchange–correlation functional[40] was applied, with a dispersion correction according to Grimme.[41] The plane-wave basis-set cut-off was set to 340 eV and all other parameters were set to the "Fine" defaults in *Materials Studio*. Unit-cell parameters were constrained to the reported values and the space-group symmetry was imposed. Neither structure produced any significant deviation on minimisation, consistent with high-quality crystal structures. The optimised structures are provided in the ESI.†

Pairwise intermolecular interaction energies were calculated using the *PIXEL* program.[30] The calculations were applied to the DFT-D minimised structures, retaining the H atom positions from those structures. The *PIXEL* output was converted to energy-vector diagrams using *processPIXEL*,[42] and subsequent visualisation was carried out in *Mercury*. The energy-vector diagrams are based on the concepts developed by Shishkin and co-workers,[43] and the approach is comparable to the energy frameworks implemented by Spackman and co-workers in the program *Crystal Explorer*.[44]

Results and discussion

Crystal structures of piracetam polytypes

FII and FIII crystallize in space groups $P\bar{1}$ and $P2_1/n$, respectively, with a single molecule in the asymmetric unit (Table 1). The structure of FII is available in the CSD in its standard reduced unit-cell setting, but it can be more directly

aligned with FIII if it is transformed using the matrix [1 0 0 / 0 −1 0 / 0 0 −1]. This produces the unit cells shown in Table 1, and the overlaid structures indicated in Fig. 2. Throughout this paper, we refer to FII in this transformed setting.

The common 2-D layers in the polytypes lie parallel to the (001) planes. Within these layers, the piracetam molecules are linked into centrosymmetric pairs through their amide groups (graph set $R_2^2(8)$), and the pairs are linked along the a axis by further N–H⋯O interactions to the carbonyl O atom of the 5-membered ring (Fig. 3). Thus, the H-bonding network defines columns of $R_2^2(8)$ dimers along the a axis. Molecules in neighbouring H-bonded columns adopt face-to-face arrangements of their rings. Along the b axis, the molecules are related by inversion centres, defining the consistent polytypic layers (Fig. 3). In FII, neighbouring layers are related by translation along the defined c axis. Molecules adopt face-to-face arrangements of rings and edge-to-edge interactions involving pairs of C–H⋯O contacts, both across crystallographic inversion centres. The rings in all piracetam molecules are approximately aligned in parallel planes. In FIII, adjacent layers are related by 2_1 screw axes parallel to the b axis, which leads to doubling of the c axis compared to FII. Neighbouring molecules adopt edge-to-face interactions between rings, involving C–H⋯O contacts, to produce a herringbone type arrangement. In terms of the C–H⋯O contacts between molecules, the alternative interlayer arrangements represent a classic "dimer *vs.* catemer" case.

Intermolecular interaction energies

The total lattice energies, calculated by *PIXEL*, suggest that FIII ($E_{latt} = -134.0$ kJ mol^{-1}) is marginally more stable than FII ($E_{latt} = -132.0$ kJ mol^{-1}).§ Lists of pairwise intermolecular interaction energies are given in the ESI.† The derived energy-vector models (Fig. 4) comprise lines linking the molecular centroids, scaled in length according to the magnitude of the interaction energy between the molecules. The most stabilising interaction in the structure is displayed as a complete line, and less stabilising interactions are scaled proportionally to produce gaps within the lines. Larger gaps indicate less stabilising interactions, and it is intuitive to see the directions in which molecules are most strongly and least strongly bound. The energies refer to the total interaction between molecules, rather than any specific interactions such as hydrogen bonds.

---

§ The DFT-D energy-minimised structures also suggest that FIII is more stable than FII, by *ca.* 1.5 kJ mol^{-1}.
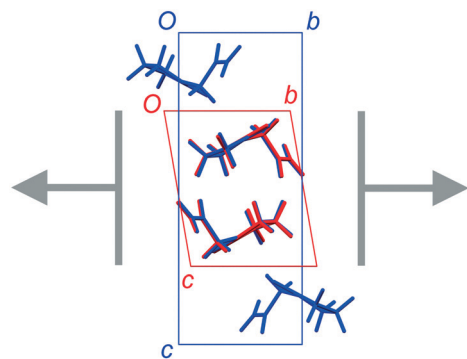
Fig. 2 Overlay of the unit-cell contents of FII (BISMEV11, red) and FIII (BISMEV12, blue). The structure of FII has been transformed compared to the version in the CSD, as described in the text. The common 2-D layers of the polytypes lie in the horizontal plane, as indicated by the arrows.
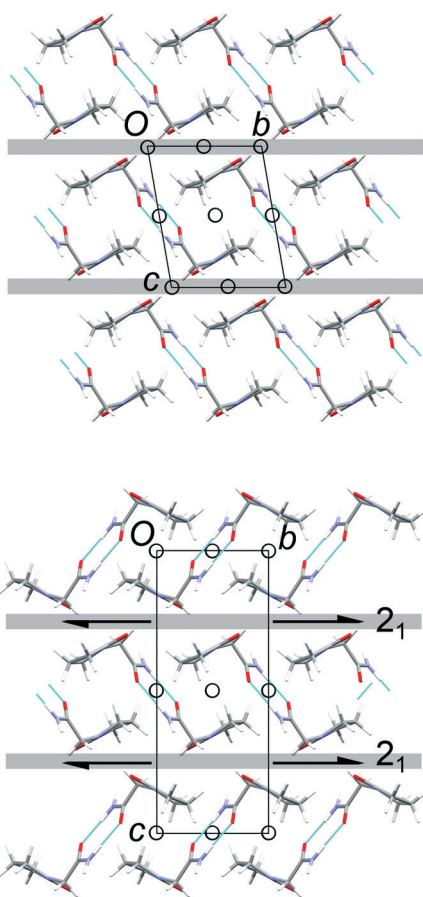

Fig. 3 Structures and selected symmetry elements of FII (top) and FIII (bottom) viewed along the *a* axis. The grey bars indicate the interlayer regions between the common polytypic layers.

Fig. 4 confirms the expectation that the most stabilising interaction in each structure occurs between molecules linked by the $R_2^2(8)$ hydrogen-bonded dimer between amide groups. This is *ca.* −64 kJ mol^{-1} in both structures, which places the two diagrams on approximately the same scale. Since FII and FIII
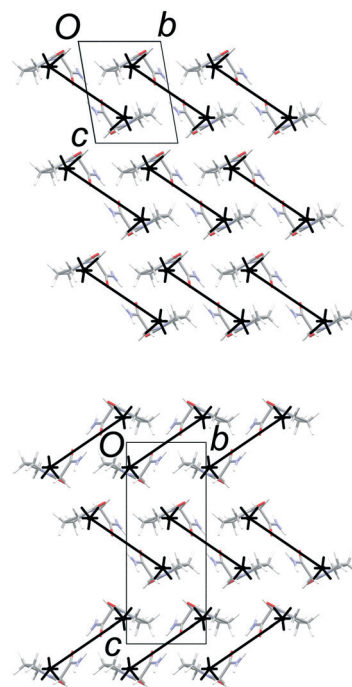

Fig. 4 Energy-vector models based on the stabilising interactions in FII and FIII. The diagrams look identical within the common 2-D layers (horizontal), but differ in orientation in neighbouring layers. Strong interactions are also formed along the *a* axis (perpendicular to the page) due to N–H⋯O hydrogen bond between molecules within the polytypic layers.

contain identical layers, the energy-vector diagrams appear identical in the *ab* planes, and the main point of interest is the difference between the interactions in neighbouring layers. To amplify these regions, the models in Fig. 5 show only the interlayer interactions, scaled to the most stabilising interlayer interaction in each case. Again, these have very similar energies (see below), so the diagrams are on a comparable scale.

The simplest interlayer arrangement is seen for form III, where there is only one type of interaction with any significant interaction energy (magnitude >3 kJ mol^{-1}). This is the edge-to-face interaction noted between rings, with total interaction energy −27.0 kJ mol^{-1}. The resulting framework in the interlayer region comprises regular zig-zag patterns along the *b* axis, confined within the *bc* planes. In form II, the noted face-to-face and edge-to-edge interactions across the interlayer region have closely comparable interaction energies (−29.8 and −29.1 kJ mol^{-1}, respectively), and adopt a similar zig-zag pattern. Some further interactions of the order of 6–8 kJ mol^{-1} are formed between molecules in adjacent *bc* planes, including one destabilising coulombic interaction at +8.0 kJ mol^{-1}. However, the overall picture in the interlayer region is very similar in FII and FIII, and there is little in the details of the energy-vector diagrams to distinguish the two cases. The picture provided in Fig. 4 is the best summary: the networks are very closely comparable, including in the interlayer region, but differ in orientation in neighbouring layers on account of the polytypism.
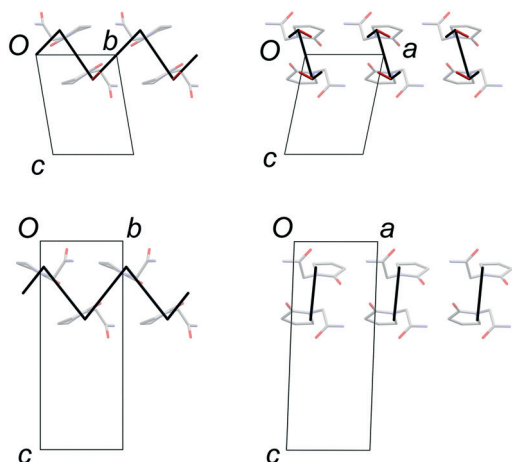
Paper

Fig. 5 Energy-vector models of the interlayer regions in FII (top) and FIII (bottom). The diagrams are scaled to the most stabilising interlayer interaction, which is approximately the same in both structures. The red line in the model for FII indicates a destabilising coulombic interaction.

Thermal expansion measurements

Lattice parameters were measured for single crystals of FII and FIII over the temperature range 100–300 K in 50 K steps (ESI†). The change in unit-cell volume over the range is effectively linear for both polymorphs. The volumetric thermal expansion coefficient (Table 2) is larger for FII (211(5) ppm K^{-1}) than for FIII (154(5) ppm K^{-1}). In the latter, the principal expansion axes are approximately aligned with the a, b and c axes of the unit cell (Fig. 6). The associated expansion coefficients (Table 2) indicate broadly isotropic expansion within the polytypic layers, with greater expansion occurring perpendicular to the layers. In FII, the principal expansion axes are not directly aligned with the unit-cell axes, but rather appear to be aligned with the piracetam molecules (Fig. 6). The axis with the largest coefficient lies approximately normal to the planes of the piracetam molecules, while that with the second largest coefficient is aligned roughly parallel to the side-on interaction involving the C–H···O contacts. For comparison with FIII, the expansion coefficients calculated for FII along the a and b axes and perpendicular to the polytypic layers (given by the change in $d(001)$) are 32, 76 and 87 ppm K^{-1}, respectively. These values indicate that the expansion of FIII is largely uniaxial, with greatest expansion perpendicular to the polytypic layers. This is the picture that might be expected from the energy-vector models in Fig. 4. In FII, however,
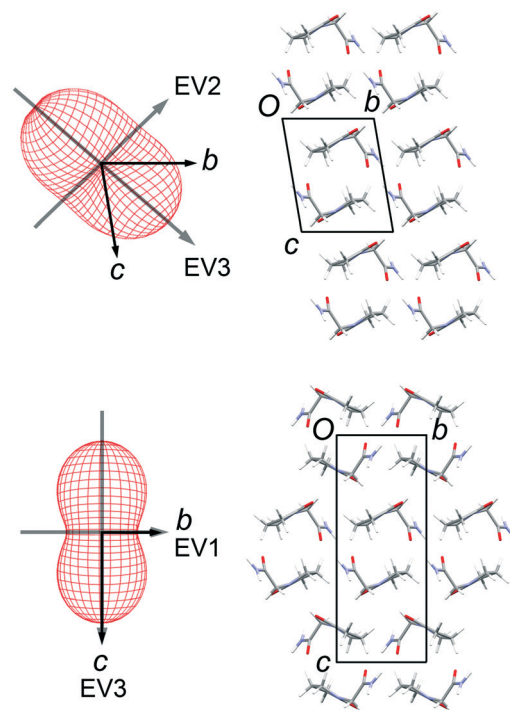

Fig. 6 Thermal expansion tensors and orientation of the principal expansion axes in FII (top) and FIII (bottom). The expansion coefficients along each axis are indicated in Table 2. The third principal axis is approximately perpendicular to the page. The axis directions are averaged over the temperature range 100–300 K.

expansion in the bc planes is closer to isotropic. Since the polytypic layers are identical in the two structures, this difference must reflect the different nature of the face-to-face *vs.* edge-to-face arrangements of the piracetam rings at the interlayer regions.

Nanoindentation

Nanoindentation was performed on well-formed single crystals of both polymorphs. While both the {001} and {10−1} faces of FII could be indented, only the {001} face of FIII was sufficiently well developed for indentation experiments (see ESI† for face identification). Representative indentation force (P) *versus* the depth of penetration (h) responses are displayed in Fig. 7. As seen, the P–h responses obtained on the {001} faces of FII and FIII are similar. However, {001} and {10−1} of FII differ substantially. All the P–h curves indicate significant plastic deformation, as inferred from the residual indentation depth upon complete unloading. Serrations on

Table 2 Thermal expansion coefficients (ppm, K^{-1}) along the principal axes of expansion in FII and FIII. Values in parentheses are standard uncertainties, obtained from a linear least-squares fit to the values obtained over each measured temperature step.[32] The axis directions are shown in Fig. 6

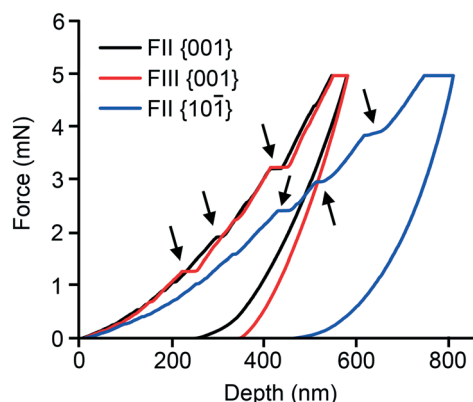|	EV1	EV2	EV3	Volumetric
FII	20 (2)	71 (2)	116 (4)	211 (5)
FIII	30 (3)	44 (1)	78 (3)	154 (5)

Fig. 7 Nanoindentation force–displacement (F–d) curves.

the loading segments (highlighted by arrows), which are often referred to as 'pop-ins' and indicate intermittent plastic deformation events, are seen in all the three P–h responses. The average values of the displacements associated with the pop-ins are often correlated with integer multiples of the relevant interplanar spacing (d_{hkl}) of the crystal structure. For FII, the pop-ins occur with approximate displacement magnitudes of 4, 8, 16 and 40 nm for {001}, and 6, 18, 24 and 36 nm for {10−1}. For FIII {001}, the magnitudes are *ca.* 8, 32 and 40 nm. These values are consistent with the expected integer multiples of the respective d_{hkl} values, as listed in Table 3.[6,7,9,45,46] The serrations on the loading segments are more pronounced for FII {10−1} and the residual depth is considerably larger. These observations generally imply that the plastic response of the FII crystal is significantly anisotropic, which is consistent with the anisotropy observed in the thermal expansion measurements. Images of the indentation impressions (ESI†) obtained on both examined faces of FII show material pile-up along two (out of three) edges, whereas pile-up occurs along all three edges of the indents made on FIII {001}. This observation implies that FIII is less anisotropic in terms of plastic flow.

Values of E and H, estimated using the Oliver–Pharr method, are listed in Table 3. Before discussing these properties, it is instructive to note that E reflects the resistance of a material to elastic deformation that recovers fully upon complete unloading (*i.e.* the shape of the material prior to deformation is completely restored).[45,46] For molecular crystals, elasticity is sensitive to the nature and number of the intermolecular interactions.[10] On the other hand, H broadly reflects the resistance of a material to plastic deformation that leads to irreversible shape change.[45,46] For

organic crystals, the presence or absence of facile slip planes in their crystal structures typically determines whether or not they are susceptible to plasticity.[47–49] Slip planes are characterised by crystallographic molecular planes with smooth topology, which are often strengthened in-plane by specific interactions such as hydrogen bonds, whereas the inter-planar interactions are weak and hence permit easy and irreversible shear sliding of the planes past each other.[50,51]

Data presented in Table 3 show that indentation on {001} yields similar H values for both FII and FIII (within the errors of the measurement), but different E values. The loading segment of the curve shows distinct pop-ins, which have also been noted for other polytypic systems, such as aspirin[6] and felodipine,[7] for indentation perpendicular to the polytypic layers. For the piracetam polymorphs, it is evident from the energy-vector models (Fig. 4) that the interlayer regions parallel to {001} are most likely to act as slip planes due to their topologically flat nature. Hence, indentation on the {001} face results in the maximum shear stress perpendicular to the slip planes. The larger value of E for FIII is nominally consistent with the smaller thermal expansion coefficient along that direction. Both indicate that the edge-to-face interlayer interactions in FIII are stiffer than the face-to-face and edge-to-edge interactions in FII. Indentation on the {10−1} face of FII yielded an E value comparable to that of {001} (within the errors of the measurement), but a significantly smaller value of H. The loading curve of {10−1} also shows slightly less well-defined pop-ins. These observations are consistent with indentation at a smaller angle relative to the suggested interlayer slip planes.

Tabletability

Tabletability, referring to the plot of tablet tensile strength (σ_c) against compaction pressure, is widely used to estimate materials performance during compression.[52] For a given pressure, a material with higher σ_c is said to have better tabletability. Fig. 8 shows that σ_c of FII is considerably better than FIII at all the studied compaction pressures and therefore exhibits better tabletability. While σ_c of both polymorphs increases linearly with F up to 100 MPa, it appears to plateau out for FIII for $F > 100$ MPa while continuing to increase for FII. Since σ_c indicates how well the particles bond together mechanically during compaction, the lower E and H of FII facilitate higher contact area between the particles (due to lower stiffness) followed by higher adhesion due to plastic flow. The face-to-face and edge-to-edge alignments of all the piracetam ring planes in form II

Table 3 Elastic modulus (E), hardness (H), indented faces, and d_{hkl} for FII and FIII

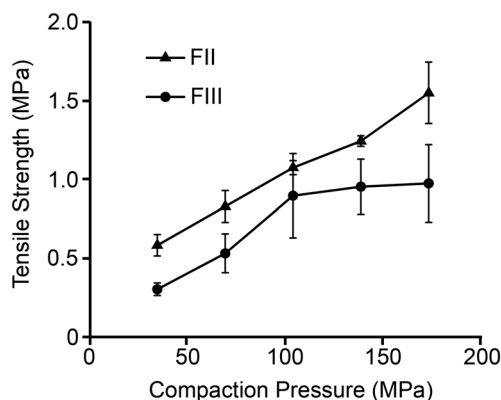| Polymorph	Indented face	d_{hkl} (Å)	Elastic Modulus (E) GPa	Hardness (H) MPa
FII	{001}	4.04	8.7 ± 0.32	513 ± 42
	{10−1}	6.07	8.1 ± 0.34	363 ± 18
FIII	{001}	8.08	10.6 ± 0.36	532 ± 29

Fig. 8 Tabletability plot of FII and FIII (n = 3 tablets at each pressure).

appears to be the structural reason for the lower E and H in FII. The herringbone type arrangement in the interlayer region of FIII, with edge-to-face alignment of molecules, imparts higher resistance to both elastic and plastic deformations. It is also noteworthy that a higher E could lead to tensile stress development at the particle interfaces during unloading and, in the process, reduce the strength of the tablet. This could be the reason not only for the lower σ_c in FIII, but also its stagnation at higher compaction pressures.

Conclusions

This analysis of the piracetam polytypes produces a plausible link between the crystal structures of FII and FIII, and their established tableting behaviour. Interaction energies and derived energy-vector models give some static indication of the nature of the intermolecular interactions, while thermal expansion measurements add a useful indicator of how the structures respond differently under stress. Alignment of the principal thermal expansion axes with the intermolecular interactions at the interface between the polytypic layers seems especially informative in this example. Nanoindentation measurements confirm the anticipated anisotropic nature of plastic deformation for FII. This analysis of piracetam adds another example to the list of polytypic structures that have been studied, whose close similarity should assist derivation of robust structure–property correlations in this type of (pharmaceutical) molecular materials.

Conflicts of interest

There are no conflicts to declare.

Acknowledgements

Notes and references

1   C. C. Sun, *J. Pharm. Sci.*, 2009, **98**, 1671.
2   C. Sun and D. J. W. Grant, *Pharm. Res.*, 2004, **21**, 382.
3   A. V. Trask, W. D. S. Motherwell and W. Jones, *Cryst. Growth Des.*, 2005, **5**, 1013.
4   K. Chow, H. H. Y. Tong, S. Lum and A. H. L. Chow, *J. Pharm. Sci.*, 2008, **97**, 2855.
5   S. Karki, T. Friščić, L. Fábián, P. R. Laity, G. M. Day and W. Jones, *Adv. Mater.*, 2009, **21**, 3905.
6   S. Varughese, M. S. R. N. Kiran, K. A. Solanko, A. D. Bond, U. Ramamurty and G. R. Desiraju, *Chem. Sci.*, 2011, **2**, 2236.
7   M. K. Mishra, G. R. Desiraju, U. Ramamurty and A. D. Bond, *Angew. Chem., Int. Ed.*, 2014, **53**, 13102.
8   P. P. Upadhyay and A. D. Bond, *CrystEngComm*, 2015, **17**, 5266.
9   S. Varughese, M. S. R. N. Kiran, U. Ramamurty and G. R. Desiraju, *Angew. Chem., Int. Ed.*, 2013, **52**, 2701.
10 S. Saha, M. K. Mishra, C. M. Reddy and G. R. Desiraju, *Acc. Chem. Res.*, 2018, **51**, 2957.
11 C. Wang and C. C. Sun, *CrystEngComm*, 2020, **22**, 1149.
12 L. J. Taylor, D. G. Papadopoulos, P. J. Dunn, A. C. Bentham, N. J. Dawson, J. C. Mitchell and M. J. Snowdon, *Org. Process Res. Dev.*, 2004, **8**, 674.
13 M. Egart, B. Janković, N. Lah, I. Ilić and S. Srčič, *Pharm. Res.*, 2015, **32**, 469.
14 M. K. Mishra, P. Sanphui, U. Ramamurty and G. R. Desiraju, *Cryst. Growth Des.*, 2014, **14**, 3054.
15 J. A. Yadav, K. S. Khomane, S. R. Modi, B. Ugale, R. N. Yadav, C. M. Nagaraja, N. Kumar and A. K. Bansal, *Mol. Pharmaceutics*, 2017, **14**, 866.
16 S. Chattoraj, L. Shi, M. Chen, A. Alhalaweh, S. Velaga and C. C. Sun, *Cryst. Growth Des.*, 2014, **14**, 3864.
17 M. Egart, I. Ilić, B. Janković, N. Lah and S. Srčič, *Int. J. Pharm.*, 2014, **472**, 347.
18 G. Admiraal, J. C. Eikelenboom and A. Vos, *Acta Crystallogr., Sect. B: Struct. Crystallogr. Cryst. Chem.*, 1982, **38**, 2600.
19 D. Louer, M. Louer, V. A. Dzyabchenko, V. Agafonov and R. Céolin, *Acta Crystallogr., Sect. B: Struct. Sci.*, 1995, **51**, 182.
20 R. Céolin, V. Agafonov, D. Louër, V. A. Dzyabchenko, S. Toscani and J. M. Cense, *J. Solid State Chem.*, 1996, **122**, 186.
21 F. P. A. Fabbiani, D. R. Allan, S. Parsons and C. R. Pulham, *CrystEngComm*, 2005, **7**, 179.
22 F. P. A. Fabbiani, D. R. Allan, W. I. F. David, A. J. Davidson, A. R. Lennie, S. Parsons, C. R. Pulham and J. E. Warren, *Cryst. Growth Des.*, 2007, **7**, 1115.
23 L. L. DeMatos, A. C. Williams, S. W. Booth, C. R. Petts, D. J. Taylor and N. Blagden, *J. Pharm. Sci.*, 2007, **96**, 1069.
24 A. Tilborg, D. Jacquemin, B. Norberg, E. Perpete, C. Michaux and J. Wouters, *Acta Crystallogr., Sect. B: Struct. Sci.*, 2011, **67**, 499.
25 M. Barrett, H. Hao, A. Maher, K. Hodnett, B. Glennon and D. Croker, *Org. Process Res. Dev.*, 2011, **15**, 681.

26 A. Maher, Å. C. Rasmuson, D. M. Croker and B. K. Hodnett, *J. Chem. Eng. Data*, 2012, **57**, 3525.

27 A. Maher, C. C. Seaton, S. Hudson, D. M. Croker, Å. C. Rasmuson and B. K. Hodnett, *Cryst. Growth Des.*, 2012, **12**, 6223.

28 A. Maher, D. M. Croker, C. C. Seaton, Å. C. Rasmuson and B. K. Hodnett, *Cryst. Growth Des.*, 2014, **14**, 3967.

29 M.-H. Chambrier, N. Bouhmaida, F. Bonhomme, S. Lebègue, J.-M. Gillet, C. Jelsch and N. E. Ghermani, *Cryst. Growth Des.*, 2011, **11**, 2528.

30 A. Gavezzotti, *New J. Chem.*, 2011, **35**, 1360.

31 C. R. Groom, I. J. Bruno, M. P. Lightfoot and S. C. Ward, *Acta Crystallogr., Sect. B: Struct. Sci., Cryst. Eng. Mater.*, 2016, **72**, 171.

32 M. J. Cliffe and A. L. Goodwin, *J. Appl. Crystallogr.*, 2012, **45**, 1321.

33 W. C. Oliver and G. M. Pharr, *J. Mater. Res.*, 1992, **7**, 1564.

34 W. C. Oliver and G. M. Pharr, *J. Mater. Res.*, 2004, **19**, 3.

35 M. S. R. N. Kiran, S. Varughese, C. M. Reddy, U. Ramamurty and G. R. Desiraju, *Cryst. Growth Des.*, 2010, **10**, 4650.

36 M. K. Mishra, K. Mishra, A. Narayan, C. M. Reddy and V. R. Vangala, *Cryst. Growth Des.*, 2020, **20**, 6306.

37 C. F. Macrae, P. R. Edgington, P. McCabe, E. Pidcock, G. P. Shields, R. Taylor, M. Towler and J. van de Streek, *J. Appl. Crystallogr.*, 2006, **39**, 453.

38 S. J. Clark, M. D. Segall, C. J. Pickard, P. J. Hasnip, M. J. Probert, K. Refson and M. C. Payne, *Z. Kristallogr.*, 2005, **220**, 567.

39 Accelrys, *Materials Studio v. 6.0*, San Diego, California, USA, 2011.

40 J. P. Perdew, K. Burke and M. Ernzerhof, *Phys. Rev. Lett.*, 1996, **77**, 3865.

41 S. Grimme, *J. Comput. Chem.*, 2006, **27**, 1787.

42 A. D. Bond, *J. Appl. Crystallogr.*, 2014, **47**, 1777.

43 O. V. Shishkin, V. V. Dyakonenko and A. V. Maleev, *CrystEngComm*, 2012, **14**, 1795.

44 M. J. Turner, S. P. Thomas, M. W. Shi, D. Jayatilaka and M. A. Spackman, *Chem. Commun.*, 2015, **51**, 3735.

45 M. K. Mishra, U. Ramamurty and G. R. Desiraju, *Curr. Opin. Solid State Mater. Sci.*, 2016, **20**, 361.

46 U. Ramamurty and J. Jang, *CrystEngComm*, 2014, **16**, 12.

47 C. Sun and D. J. W. Grant, *Pharm. Res.*, 2001, **18**, 274.

48 P. Upadhyay, K. S. Khomane, L. Kumar and A. K. Bansal, *CrystEngComm*, 2013, **15**, 3959.

49 M. K. Mishra, U. Ramamurty and G. R. Desiraju, *J. Am. Chem. Soc.*, 2015, **137**, 1794.

50 K. S. Khomane and A. K. Bansal, *J. Pharm. Sci.*, 2013, **102**, 4242.

51 K. S. Khomane, P. K. More and A. K. Bansal, *J. Pharm. Sci.*, 2012, **101**, 2408.

52 E. Joiris, P. D. Martino, C. Berneron, A.-M. Guyot-Hermann and J.-C. Guyot, *Pharm. Res.*, 1998, **15**, 1122.